Phased Array Ultrasonic Testing for Post-Weld and OnLine Detection of Friction Stir Welding Defects

D. J. Huggett, M. W. Dewan, M. A. Wahab, A. Okeil & T. W. Liao

Phased Array Ultrasonic Testing for Post-Weld and OnLine Detection of Friction Stir Welding Defects

D. J. Huggett[a], M. W. Dewan[a], M. A. Wahab[a], A. Okeil[b], and T. W. Liao[a]

[a]Department of Mechanical and Industrial Engineering, Louisiana State University, Baton Rouge, Louisiana, USA; [b]Department of Civil and Environmental Engineering, Louisiana State University, Baton Rouge, Louisiana, USA

ABSTRACT

Nondestructive evaluation (NDE) techniques of phased array ultrasonic testing (PAUT) and digital X-ray radiography were employed on friction stir (FS)-welded Aluminum Alloy (AA)-2219-T87 specimens. PAUT intricacies required for scanning of FS-welded specimens with a 10-MHz 32-element transducer are discussed. The time corrected gain (TCG) calibration is required for scanning with an increase in index offset to compensate for decrease in A-Scan signal peak amplitude. Calibration techniques to find small defects with appropriate size tolerances are also established. The NDE technique of digital X-ray radiography is compared to PAUT, where it was found that a calibrated PAUT system is able to discover defects less than 0.2 mm where X-ray radiography could not. Incomplete penetration (IP), wormhole (WH), surface cavity (SC), and internal void (IV) defects are analyzed. Furthermore, an online PAUT system for FSW has been developed and successfully tested. The work provided herein will provide a gateway for an ultimate goal of an automated PAUT online sensing system.

1. Introduction

Welding technology has evolved in the recent decade with the introduction of friction stir welding (FSW). As a solid state welding process, it has become increasingly popular with government research organizations and private sectors, specifically in the welding of aluminum alloys (AA) for aerospace applications. Formerly, fusion welding was the most prevalent process in the aerospace industry; however, fusion welding of aluminum caused defects such as porosity, weld metal solidification cracking, and heat-affected liquation cracking. FSW is now the leading technique which has overcome the problems of porosity and hot-cracking encountered in fusion welding of AA [1]. Nevertheless, even with these desirable qualities, fundamentally with any welding technique welding defects will occur if conducted indecorously. For this reason, nondestructive inspection techniques are always employed post-weld to determine weld defects [2].

CONTACT M. A. Wahab ✉ wahab@me.lsu.edu Department of Mechanical and Industrial Engineering, Louisiana State University, Baton Rouge, LA 70803, USA.

Color versions of one or more of the figures in the article can be found online at www.tandfonline.com/urnd.

Two major post-weld nondestructive evaluation (NDE) techniques are X-ray radiography and phased array ultrasonic testing (PAUT). These NDE techniques are required to have high reliability and accurate defect-sizing capabilities [2] in order to successfully evaluate welded structures, especially in the aerospace industry. Though these two techniques are the focus of this study, it should be noted that another emerging technology that is being evaluated for post-weld inspection on friction stir (FS) welds is the Eddy current technique [3–11]. In ultrasonic testing (UT), ultrasonic waves are scattered by planar and volumetric defects. Partially closed cracks are also detectable by ultrasonics, provided that appropriate procedures are used [12]. Alternatively, X-ray radiography utilizes a radioactive source that emits X-rays onto a specimen. A consequent X-ray image is created which depends on the degree of penetration from the high energy wave. X-ray radiography offers a fast and permanent defect image; however, the process requires access to both sides of the evaluated part and, more importantly, poses health issues which require the area near the test-location to be quarantined. Due to these inherent limitations, UT has been the preferred method over X-ray radiography for general post-weld inspections [2].

As technology for UT improved, PAUT has replaced the conventional ultrasonic methods as well as other nondestructive testing (NDT) techniques in many post-weld evaluation applications [13–17]. PAUT offers increased inspection sensitivity and coverage as well as decreased inspection times. Phased array ultrasonic probes utilize an array of piezoelectric elements which generate sound waves, typically in the MHz region. The sound waves, based upon the firing sequence of the piezoelectric elements, form a wave front that is characterized by Huygen's interference patterns [18,19]. The sound waves are predictable due to classical physics phenomena and have been well documented as they pertain to ultrasonics, as seen in [20–28].

PAUT allows the operator to better determine the size, shape, and orientation of a defect better than traditional pulse echo techniques [29–31]. Even though this technology is applied quite extensively, literature has little documentation of the intricate details needed to accurately operate a PAUT system to precisely determine the size and location of a defect, especially in FS welds. Schneider et al. [16] conducted an extensive study comparing operators of PAUT and conventional UT. The study concludes that there is variability in ability of PAUT operator's flaw sizing; consequently, it is recommended that adequate training is employed for PAUT operators. There are three levels of certification of NDT methods including level I, level II, and level III. NDT training is based upon the NDT Body of Knowledge (BOK) and can be found in the ANSI/ASNT American National Standard CP-105, ASNT Standard Topical Outlines for Qualification of Nondestructive Testing Personnel.

To the knowledge of the authors, the only article in the open literature that compares the performances of two most common NDT techniques including X-ray radiography and PAUT in detecting defective FS welds is Li et al. [30]. However, only limited information was given pertaining to the capabilities of PAUT and X-ray radiography in detecting various forms of defects. In another study [6], several NDT techniques including conventional and pulsed eddy current testing, laser generated, and phased array UT are compared in inspection of incomplete penetration discontinuities in FS butt welds. Comparisons of the two most common NDT techniques (i.e., PAUT and X-ray radiography) in detecting various forms of FS weld defects are carried out in the current article. Furthermore, the authors are not aware of any attempt to use PAUT in an integrated online manufacturing process. Such use requires operating PAUT in high temperature (HT) environments, which the authors could not find to be documented in the open literature as there are many challenges due to the damage that may incur to the sensitive piezoelectric elements. In the present study, a PAUT system developed to evaluate FS welds online is presented.

In summary, the major contributions of this article include as follows: (1) providing details of PAUT including calibration techniques, index offset considerations, and defect-size limitations pertaining to FSW, (2) carrying out a more extensive study to compare the performances of PAUT and X-ray radiography in detecting various forms of defective FS welds, and (3) designing a system to employ PAUT online for detecting defective welds.

2. PAUT and FSW experiments

Through an extensive study conducted at the NASA Michoud Assembly Facility in New Orleans, LA, AA panels were FS welded in a typical butt-joint configuration [32]. The welded specimens from that study were thereby utilized for all PAUT experiments. Through the course of the work, an OmniScan MX2 data acquisition unit [33] was utilized with a 10-MHz 32-element transducer. In the literature, PAUT has been applied to detect flaws in FS welds after welding; however, details regarding calibration and other settings are often left out [11,19,20]. In this study, a detailed analysis of these techniques was conducted to determine the best practices for utilizing PAUT on FS welds, with a mindset to scan real-time during welding. Consequently, the transducer was tested for accuracy, defect size limitations, gain effect on A-scan amplitude for various defect sizes, and specific FS weld configuration limitations. Aside from employing typical calibration procedures for PAUT systems including sensitivity, velocity, and wedge, the time corrected gain (TCG) calibration was utilized as well.

In FSW, there are two sides of a welded specimen, which are distinctively different from one another, called Advancing and Retreating. Each side of a FS weld has specific properties based upon material flow due to the rotation of the pin. Through this study, scanning of FS welded panels was conducted by placing the PAUT probe/wedge unit on the advancing side (AS) of the FS weld, as seen in Fig. 1. As defects in FSW typically form on the AS, the wedge/transducer unit was thereby placed on that side. This allows defect signals to be closer to the wedge causing less divergence of the sound waves, and thus more accurate data. Furthermore, during welding material expulsion out of the weld seam (considered flash) can occur. The expulsion of material typically occurs on the retreating side (RS), and to avoid flash contact with the wedge, the AS was deemed more suitable for placement. As the project aims to scan FS welds online, index offset is particularly important. As the FSW process generates ripple patterns on the surface of the welded area, PAUT cannot scan on top or near the weld center line without post-processing. By utilizing correct index offset processes, scanning may be accomplished without post-processing of the welded seam. Through the course of the work, the PAUT system was calibrated to be 20 mm away from the weld center line.

An important consideration for online inspection is the ability to decipher the scan images an OmniScan produces. For S-scan images, PAUT software utilizes a mirroring image technique when multiple legs (nomenclature for wave reflections by the walls of the specimen) are viewed. Sound waves which are not reflected by the defect will travel farther, and thereafter will be reflected by the back-wall of the workpiece. Utilizing multiple legs allows the scan images to illustrate waves that travel
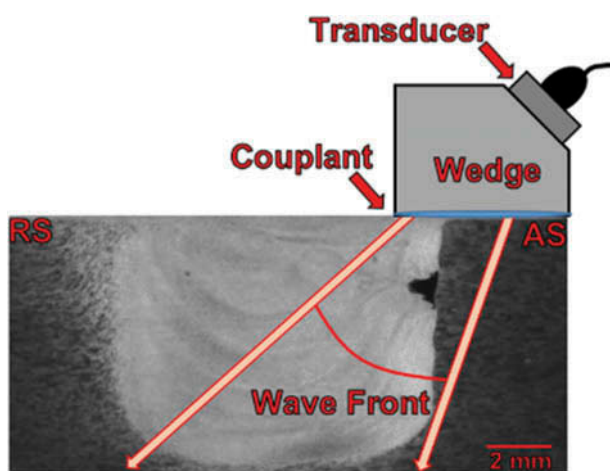
Figure 1. A typical probe and wedge configuration with illustration of wave propagation inside a FS welded specimen.

farther than the initial thickness of the workpiece. With two legs, waves travel twice the thickness of the material. This feature is very important as index offset is utilized in this study. An illustration of the inverting (mirror) image technique in the data acquisition unit with first and second leg sound waves can be seen in Fig. 2.

It can be seen that the initial defect image is at a depth of 7.3 mm in Fig. 2(a). An apparent second defect at a distance of 9.4 mm is also observed. The second defect image is located at a distance that exceeds the thickness of the workpiece (8.32 mm thickness for this experiment). The defect's actual depth is evaluated by the operator taking the difference of the depth given from the image and workpiece thickness. The resulting value is then subtracted from the workpiece thickness, which is the location similar to the first leg defect depth. In summary, due to the many elements in a PAUT transducer, signals emitted from certain elements may not be influenced by a defect; consequently, the first leg signals from those elements have not been redirected. These signals are then reflected off the bottom surface of the specimen which redirects the signal that results in reflecting off the defect. This is illustrated in Fig. 2(b) for the defect at the larger depth.
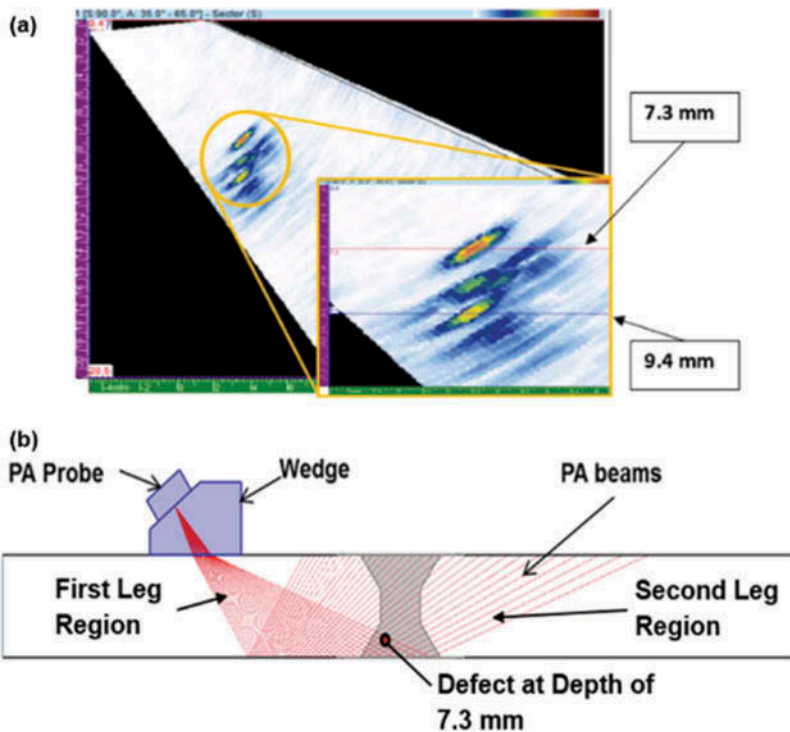

Figure 2. (a) PAUT S-scan image displaying the effect of side drilled hole (SDH) at larger depth, with associated schematic of first and second legs with SDH defect (b).

## 3. PAUT versus X-Ray radiography for post-weld inspection

A comparison of the abilities of PAUT and X-ray radiography to detect various forms and sizes of defects in weldments has been carried out in this study. The FS-welded plates were analyzed employing PAUT and compared with X-ray radiography to illustrate sizing capabilities when utilizing a calibrated PAUT system (note the X-ray images below are inverted for better quality). These FS welds were executed utilizing varying weld schedule parameters (plunge or forge force, travel speed, and spindle speed). Weld schedules were designed in a way to purposely produce defects. Four defect types are presented below. Defects presented in this study include surface cavities (SC), wormhole (WH), internal voids (IV), and incomplete penetration (IP). SCs are surface defects whereas WH and IV are internal defects. IP is a defect located at the root of a weld caused by unconsolidated material on the seam line. Each defect type has a different formation mechanism and is directly related to the process parameters utilized during welding. First, a SC formed by lack of material in the weld seam during the plunge stage of FSW is presented. Secondly, a WH defect is presented, followed by another SC, often considered a trenching (TR) defect. Following these defects, an IV is presented. Lastly, IP defects are described. General defect locations of a FS weld can be observed in Fig. 3, with anticipated ultrasonic wave front, or leg, which will identify the defect.

Figure 4 illustrates an FS weld that has incurred a large defect located on the AS of the weld. An A-scan image can be seen with the associated S-scan image. The S-scan image depicts a snapshot of the defect with accurate estimates of its size and location. It is observed that the defect is found by second leg signals, as the depth of the defect is greater than the workpiece's thickness, i.e., 8.32 mm, and less than doubled thickness, i.e., 16.64 mm. Figure 5 illustrates a representation of the X-ray image compared with a B-scan and a C-scan of the PAUT system. Furthermore, in Figs. 6 and 7, a WH defect is shown. In a similar fashion, a SC defect is
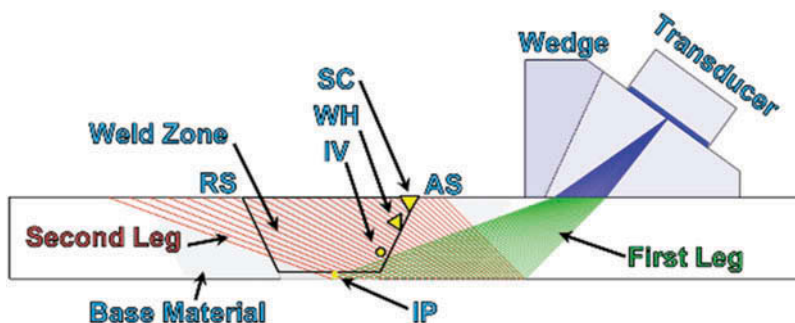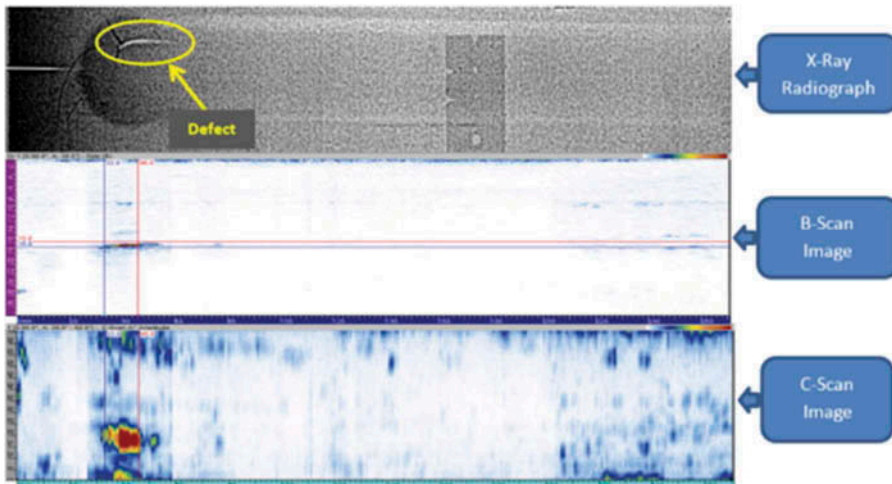

Figure 3. Illustration of the PAUT system with various legs indicating where FSW defects may occur.
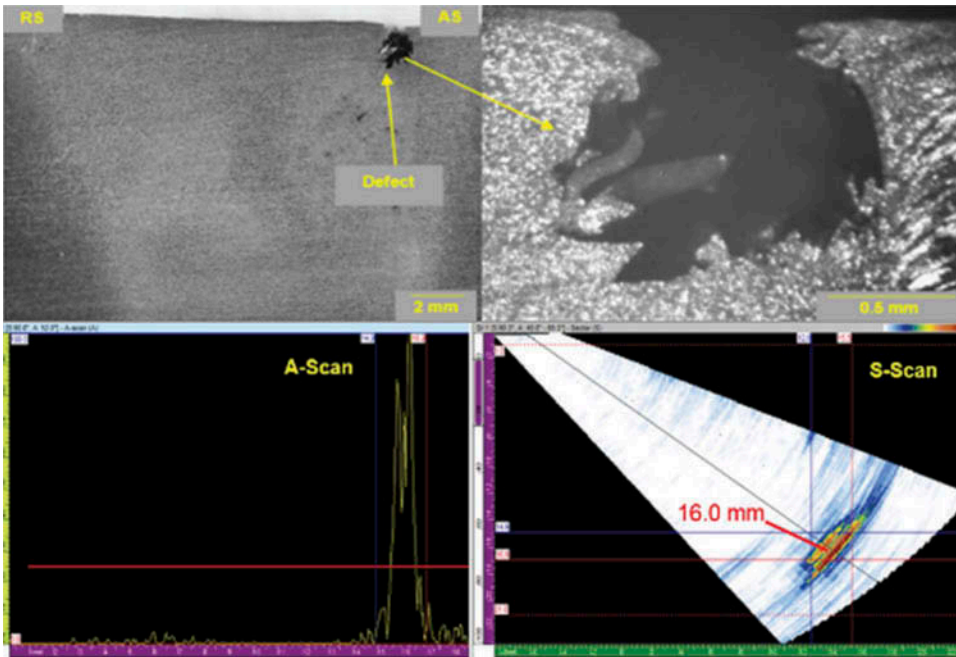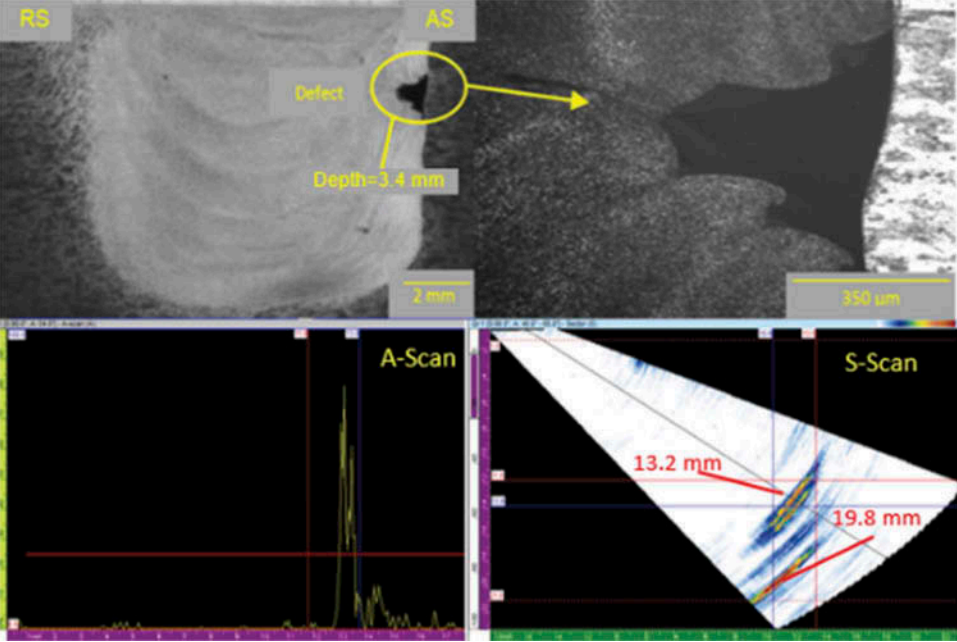
Figure 4. Optical image of cross-section, enlarged defect image, PAUT A-scan, and S-scan image (second leg) of an FS-welded panel with surface cavity (observed by second leg).

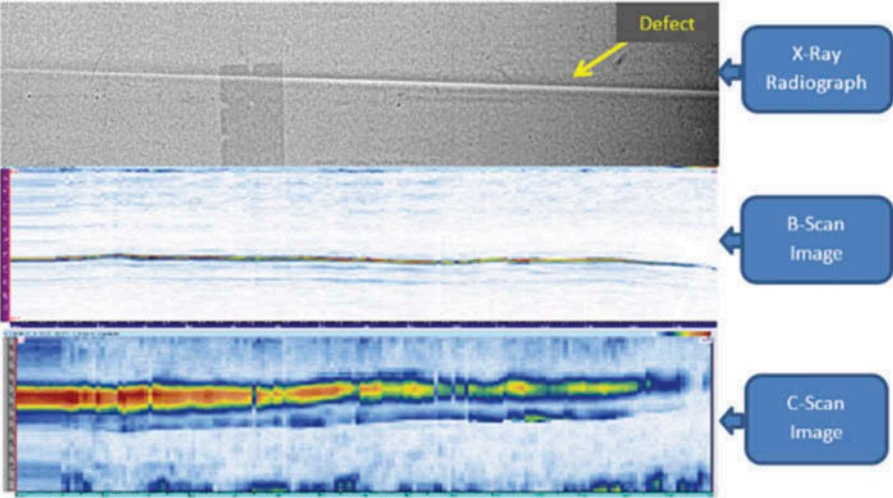**Figure 5.** Radiographic, PAUT B-scan, and PAUT C-scan images of an FS-welded panel with surface defect.

presented in Figs. 8 and 9. These defects were as well detected by the second leg signals, as the wedge/transducer system is not scanning near or on top of the defect. In Fig. 6, it is noted that the WH was also found by third leg signals, as the defect's depth is greater than 16.64 and less than
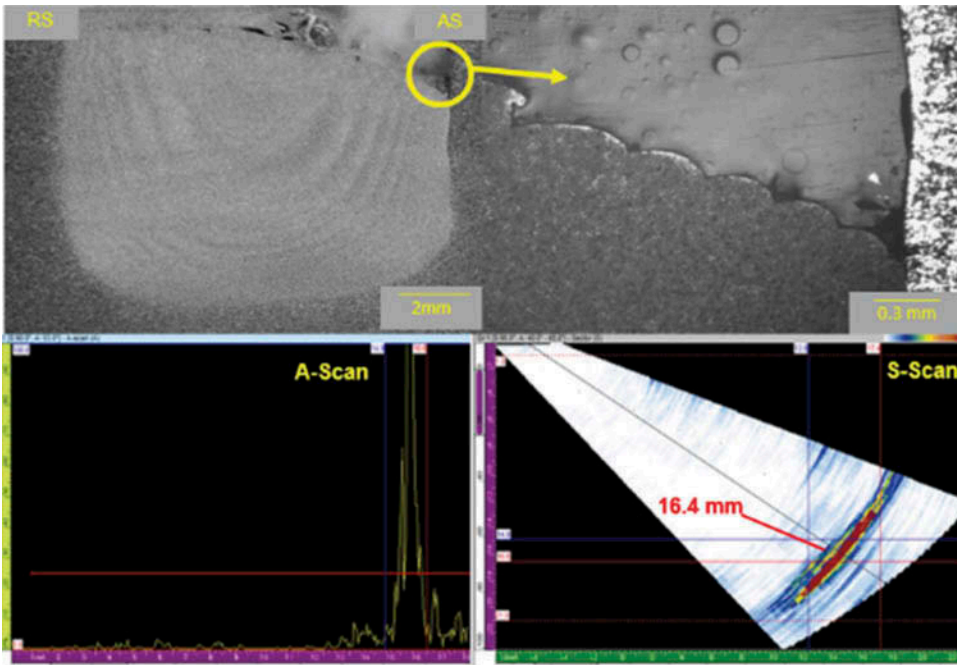
Figure 6. Optical image of cross-section, enlarged defect image, PAUT A-scan, and S-scan image of an FS-welded panel with wormhole defect (observed by second and third leg).
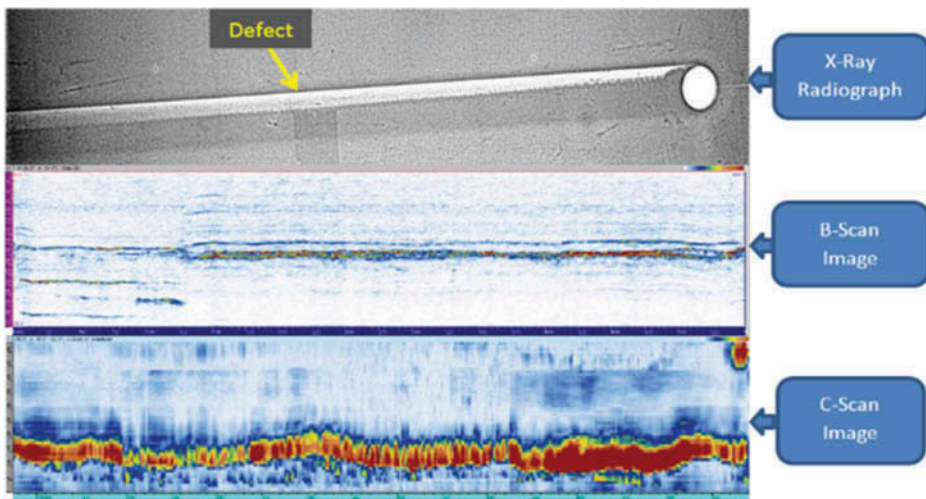

Figure 7. Radiographic, PAUT B-scan, and PAUT C-scan images of an FS-welded panel with wormhole defect.

24.96 mm. It can be seen that, as the signal propagates further through the specimen, the defect depth has larger error. These defects were found accurately with X-ray radiography and PAUT. Note that there was no post-processing of the panels for these tests. The X-ray image compares

Figure 8. Optical image of cross-section, enlarged defect image, PAUT A-scan, and S-scan image of an FS-welded panel with SC defect (observed by second leg).

Figure 9. Radiographic, PAUT B-scan, and PAUT C-scan images of an FS-welded panel with SC defect.

very well with PAUT scans and shows that the two NDE techniques correlate very well for large defects, which is expected; however, it can be said that defects of this size and shape will most likely not occur in the production line.
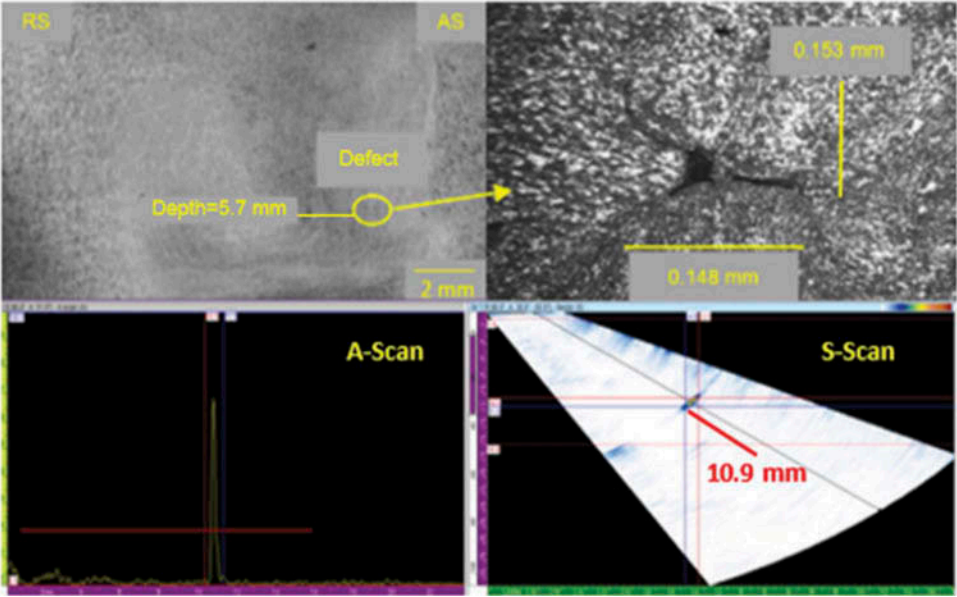
Figure 10. Optical image of cross-section, enlarged defect image, PAUT A-scan, and S-scan image of an FS-welded panel with internal void (observed by second leg).

An internal void defect is shown in Figs. 10 and 11. In this FS weld, two defects were found by the PAUT system; however, both defects were not found by X-ray radiography. The smaller defect on the right in Fig. 11 is analyzed here. The defect was measured to be in the range of 0.15 mm in both length and height. It is seen that the A-scan amplitude does not reach 80% due to calibrating the system with a larger defect size. The intensity of the reflected sound wave decreased giving maximum amplitude of 68%. It is observed that the X-ray image does not detect the small defect.
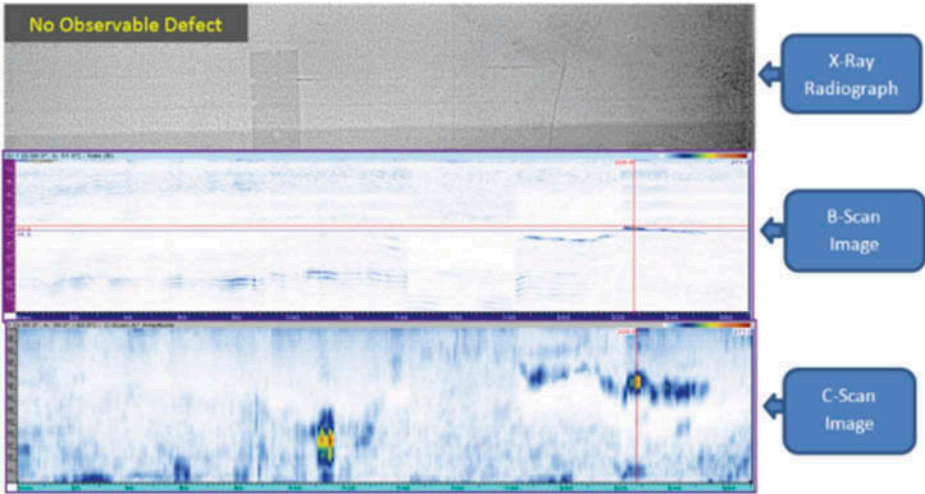
Figure 11. Radiographic image, PAUT B-scan image, and C-scan image of an FS-welded panel with internal void.

One challenging defect for NDE techniques to observe is IP. As this defect can be detrimental for industrial applications, many studies have analyzed said defects for all major welding processes; however, few pertaining to IP for FSW by employing ultrasonic techniques can be found in the open literature. Lamarre et at. [34] employed a triple NDT approach including ultrasonic pulse echoes, ultrasonic attenuation measurements, and eddy currents to analyze FS-welded specimens. It is stated that the triple NDT technique detects FSW defects including kissing bonds. Alternatively, it was shown that ultrasonic C-scan images are difficult to observe IP; however, utilizing a noise ratio of parent and weld material, a better indication of IP can be obtained. A high noise ratio indicates a kissing bond is present. Mandache et al. [6] compared multiple NDE techniques (pulsed eddy current, conventional eddy current, PAUT, laser-generated ultrasonic waves with synthetic aperture focusing technique [SAFT], liquid die penetrant) to analyze IP defects where a retractable pin tool was employed to vary the depth of penetration on a 2.56 mm-thick panel. Employing a 10-MHz 16-element probe, it was possible to detect IP defects with lengths greater than 0.2 mm from the root of the weld. In their study, however, post-processing of FS-welded specimens was conducted, whereas in our study no post-processing was carried out in order to correlate with online scanning. Bird et al. [35] developed a method to determine the forging depth of FS welds by material noise ratio analysis, which was able to measure penetration better than 0.5 mm. Furthermore, in that study it was stated that, employing ultrasonic amplitude rejection for conventional defects, it was possible to discover voids with a through wall size of 0.1 mm. A study by the same research group of the previous study developed statistical signal processing algorithms [36], which have the ability to identify weld nugget and root. Laser ultrasonics composed of a Nd:YAG laser in conjunction with a photorefractive interferometer was employed in [37] to detect internal defects and residual stresses. It was shown that such system can detect IP defects as well.

Throughout the FS experimental program carried out in our research, multiple IP defects were found, as can be seen in Table 1. In the present study, X-ray radiography had difficulty in detecting IP defects. Alternatively, PAUT was able to discover IP defects; however, an increase in gain value was needed in order to provide A-scan signal peak amplitude values near acceptable limits with the aforementioned calibration, which originally allowed 80% A-scan peak amplitude for 0.79 mm defects. Even with the increase in gain, the signal-to-noise ratio of the system was still adequate to accurately observe defects. A few IP defects could not be discovered by the PAUT system, not because of the length of the defect, but rather due to large defects also present in the same specimen (WH and SC). As the gain values were increased, large wormhole or trench defects caused high noise, and in some cases would distort the location where the IP defect resided. This should not

Table 1. Various IP defects with defect height from root of weld.

IP Height from Weld Root [μm]
614
965
480
901
753
332
433
757
454
963

be considered as a limitation on PAUT defect detection capabilities since such workpieces would be rejected due to the other defects, which are PAUT detectable. However, with the current PAUT calibrated, system IP defects with defect height less than 0.3 mm could not be detected.

To indicate the performance of the PAUT system, a comparison of an S-scan IP image with associated optical micrograph can be observed in Fig. 12. The defect size of this specimen is 480 μm and was found by the PAUT system to have a defect height of 500 μm. PAUT defect height overestimates the actual defect height in most cases due to high gain values implemented in calibration. IP defects were thereafter verified with tensile tests, which were conducted on all specimens welded in this study with an MTS 810 Material Testing System. Figure 13 illustrates an IP defect with associated fracture origination from tensile test, and scanning electron microscopy (SEM) image of the fracture surface. In the SEM image, it is evident an unbonded surface is present by observing a lack of fracture dimples associated with a bonded surface.
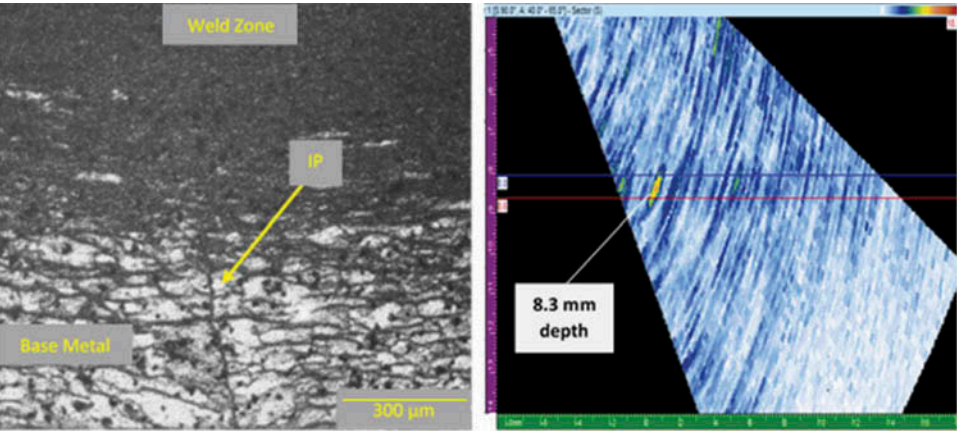
Figure 12. Optical image (left) of IP defect of length 480 μm and associated S-scan image (right) of IP defect.
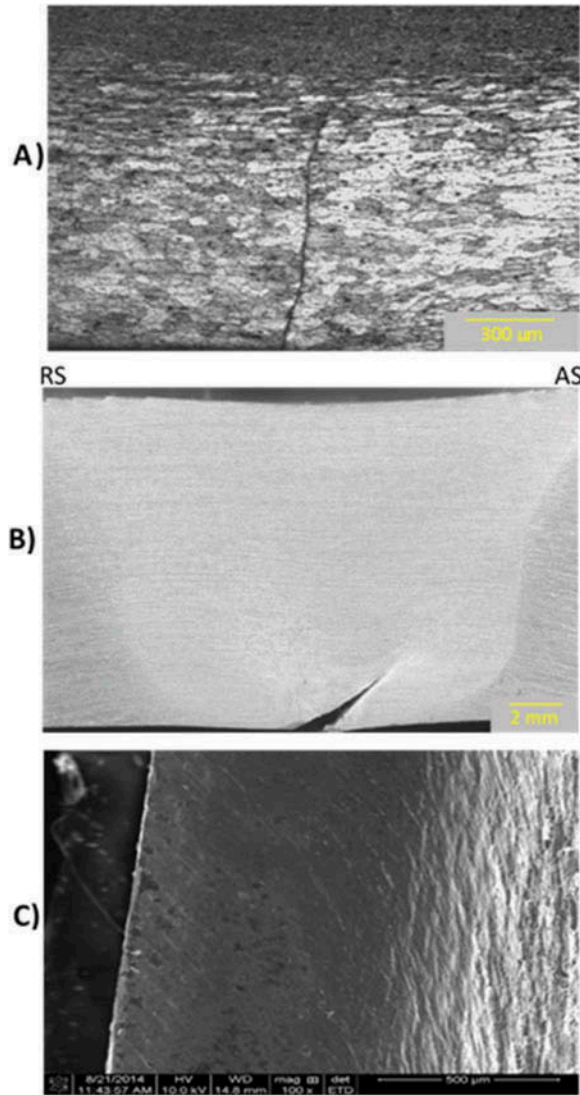
Figure 13. A) Optical micrograph of IP defect. B) Optical image of tensile tested specimen indicating fracture origination. C) SEM image indicating unbonded area.

4. Online PAUT

The ultimate goal of this study is to develop an online PAUT system that can detect various FSW-associated defects in real time, thus expediting the inspection process and any remedy measures that need to be taken such as adjusting weld schedules. There are many challenges in the path to developing such an online system. This section addresses major challenges that were investigated as part of this study, namely, HT and geometric constraints due to weld fixtures. Finally, a demonstration of the proposed system is presented for some preliminary welds.

4.1. *HT ultrasonics*

HT studies on material velocity effects for PAUT on AAs for practical applications are, to the authors' knowledge, not readily available in open literature. Presented here is a review of the few works that have been obtained. An early investigation of steels at HTs was conducted in [38] utilizing conventional ultrasonic techniques. At 400°C, a system was created to mount piezoelectric arrays on steel in an industrial plant. It is stated that the system effectively detected 1 mm side drilled holes at room temperature and 400°C. Subbaratnam et al. [39] investigated ultrasonic time of flight diffraction (TOFD) in austenitic stainless steel. TOFD tests evaluated at 149.85°C resulted in degradation of ultrasonic signals, which was compensated with an increase in gain values above what was required at ambient conditions. Similar trends were observed in Johnson et al. [40], in which various AAs (AA-1100, AA-2024-T351, AA-6061-T6, AA-7075-T6) longitudinal ultrasonic velocities were measured as temperature of the specimens was increased to solidus temperature. The work employed a Nd:YAG laser with pulses of 15 ns with energy 700 mJ to excite ultrasonic waves. It is stated that at HTs (approximately greater than 400°C) linear temperature dependence deviates. Development towards creating a flexible transducer array at 150°C was conducted in [41]. A study by Tariq et al. [42] examined various AAs including AA-2219, which illuminated that UT can be conducted to correlate hardness values to material velocity and attenuation. The study states that AA-2219 with peak hardness (HV) of 138 correlates with peak a longitudinal velocity of 6.354 mm/μs.

Employing the knowledge gained from the post-weld FSW analysis, a method to incorporate FSW working conditions was employed for real time PAUT scanning. First, PAUT transducers are quite sensitive to heat. Typically the elements in a transducer are warranty rated by the manufacturer from 5°C to 45°C. This is a leading cause why PAUT is seldom employed for HT applications. Consequently, as mentioned in the literature, a change in temperature will cause a change in the ultrasonic velocity, which poses issues for accurate defect detection. For this reason, experiments were conducted to determine approximate temperature ranges near the weld seam during FSW tests. K-type thermocouples and infrared imaging techniques were employed and determined a maximum temperature of 312°C was reached 20 mm away from the weld seam for the welding configuration. Consequently, to circumvent these HTs in order to prevent damage to the sensitive piezoelectric elements a wedge was designed by the authors and fabricated from vespel material (temperature rated: 287.8°C constant to 482.2°C intermittent) by Sonatest. As this material is rated near the eutectic melting temperature of binary aluminum-copper alloys (548°C [43]), this material was deemed suitable

for the FSW application. The wedge was further designed with a water inlet and outlet for cooling around the transducer casing to ensure piezo-electric element safety. Furthermore, inlets were inserted to allow a steady flow of couplant to the workpiece during scanning, see Fig. 14.

The effectiveness of the newly designed and fabricated wedge was first tested in a laboratory setting for a simulated controlled environment at ambient and elevated temperatures (25.0°C, 100°C, 200°C, and 300°C). The experiments entailed three trials per temperature, and utilized a different calibration file for east trial. Temperature readings were taken with K-type thermocouples and Midi Logger GL820 acquisition system with a sampling rate of 200 ms. A Thermo-Scientific 2200 Hot Plate was employed to heat the AA-2219-T87 material used for calibration. In order to pump coolant and couplant through the wedge by the inlets and outlet channel, two Master-Flex pumps were employed. Couplant is required to induce transmission of ultrasonic waves from wedge to workpiece, and the coolant is required to maintain a safe operating temperature for the piezoelectric elements in the transducer. Figure 15 illustrates the experi-mental setup. Table 2 summarizes results at ambient conditions. It is observed that with appropriate calibration procedures accurate defect sizing and location were obtained, similar to conventional PAUT wedges. The effects at elevated temperatures can be seen in Table 3. Figure 16 illustrates two S-scan images of a similar defect at varying temperatures (ambient and 300°C). It was observed that the location of the defect increased in distance as the temperature increased, due to the change in ultrasonic velocity as the material heats. It is observed that at 300°C the maximum depth change was found to be 1.2 mm. This value appears small and indicates that at 300°C there is minimal change for our PAUT configuration. One reason for this small change is due to the unconven-tional wedge material that is utilized. According to ASME standard [44], high-temperature materials up to 540°C can be measured with appropriate HT instruments. For steel, it is claimed the rule of thumb for apparent
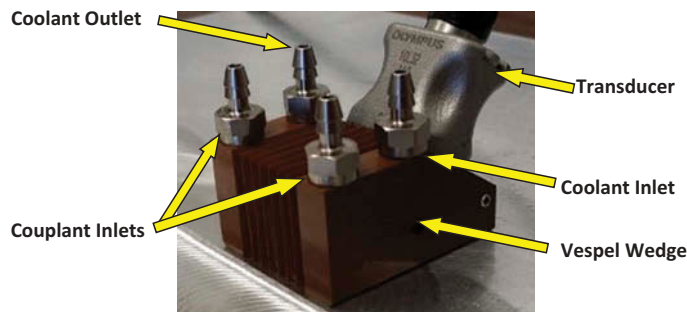
**Figure 14.** Custom PAUT HT wedge/transducer unit.
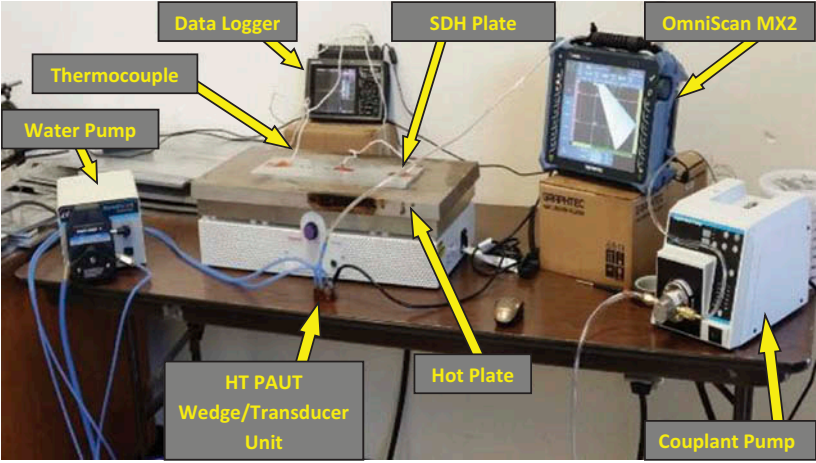
Figure 15. Illustration of HT PAUT for SDH AA-2219 specimen of 8.13 mm thickness.

Table 2. Accuracy and precision of PAUT HT transducer/wedge unit at ambient temperature.

| Actual Dia. (mm)	Measured Dia. (mm)	Δ Dia. (mm)	Actual Depth (mm)	Measured Depth (mm)	Δ Depth (mm)
1.19	1.20	0.01	2.69	2.8	0.11
	1.20	0.01	5.15	5.3	0.15
	1.20	0.01	6.30	6.30	0.00
0.79	0.90	0.11	2.83	3.00	0.17
	0.89	0.10	5.20	5.20	0.00
	0.90	0.11	7.10	7.30	0.20

Table 3. Comparison of two SDHs at increasing temperatures.

Actual Dia. [mm]	Actual Depth [mm]	Temperature [°C]	Measured Depth [mm]	Measured Dia. [mm]	Δ Depth [mm]	Δ Dia. [mm]
0.79	2.83	100	3.50	1.10	0.67	0.31
	5.20		5.70	1.30	0.50	0.51
	7.10		7.60	1.40	0.50	0.61
	2.83	200	3.70	1.00	0.87	0.21
	5.20		5.90	1.00	0.70	0.21
	7.10		8.00	1.20	0.90	0.41
	2.83	300	3.70	1.20	0.87	0.41
	5.20		5.90	1.20	0.70	0.41
	7.10		8.20	1.40	1.10	0.61
1.19	2.69	100	3.20	1.20	0.51	0.01
	5.15		5.40	1.60	0.25	0.41
	6.30		6.80	1.80	0.50	0.61
	2.69	200	3.70	1.30	1.01	0.11
	5.15		5.80	1.40	0.65	0.21
	6.30		7.40	1.40	1.10	0.21
	2.69	300	3.60	1.40	0.91	0.21
	5.15		6.20	1.50	1.05	0.31
	6.30		7.50	1.50	1.20	0.31
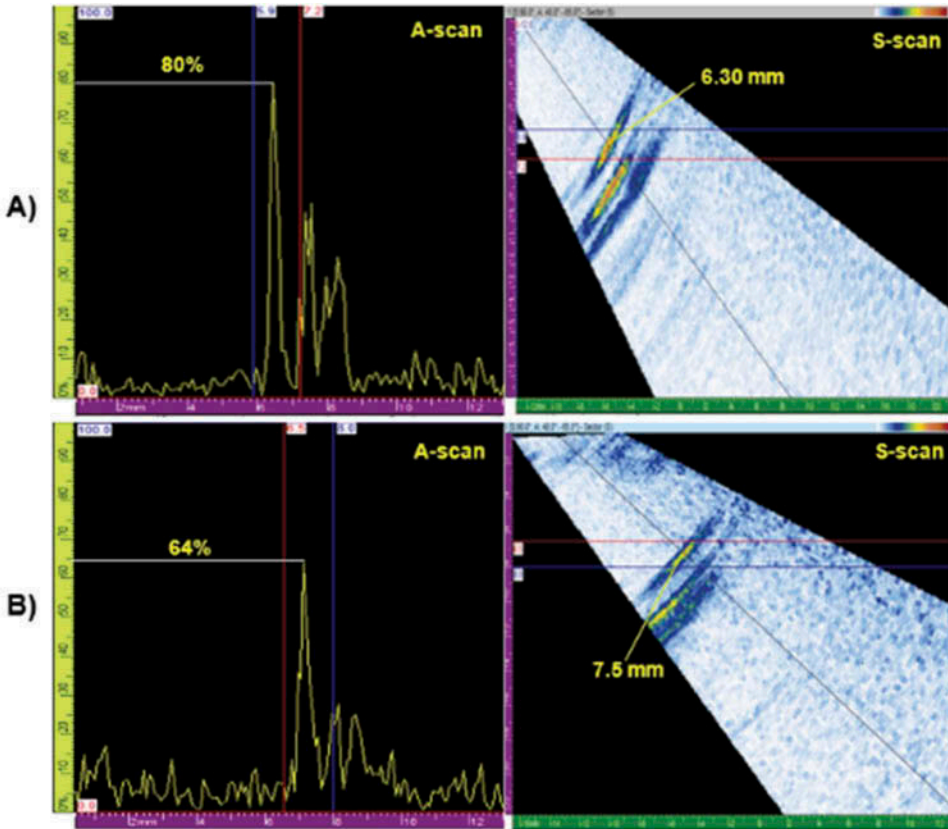
Figure 16. Comparison of A- and S-scan images of 1.19 mm diameter SDH at a depth of 6.3 mm. Case A) was conducted at room temperature, and case B) was conducted at 300°C. A change in depth of 1.2 mm occurred with an increase in temperature to 300°C with an increase in attenuation (80% down to 64% A-scan peak amplitude).

thickness measurements with elevated temperatures increases by a factor of 1% per 55°C. A comparison of defect depth variation with temperature can be seen in Fig. 17. At room temperature, error in depth measurement is small compared to when an increase in temperature occurs. With an increase in temperature, defect depth increases. Defect depth measurement variation also increases when the temperature and defect location increases. Furthermore, the attenuation has increased at higher temperatures, which can be observed by the reduction in A-scan peak amplitude. At room temperature, 80% A-scan peak amplitude (as calibrated) is obtained, whereas at 300°C, a decrease in A-scan peak amplitude is obtained; consequently, the gain value should be increased to compensate for the loss in signal intensity. When a material's temperature increases, the atoms inside are in an elevated energy state which increases interatomic spacing which impedes transmission. Consequently, at these temperatures a calibration of the software must take place in order to
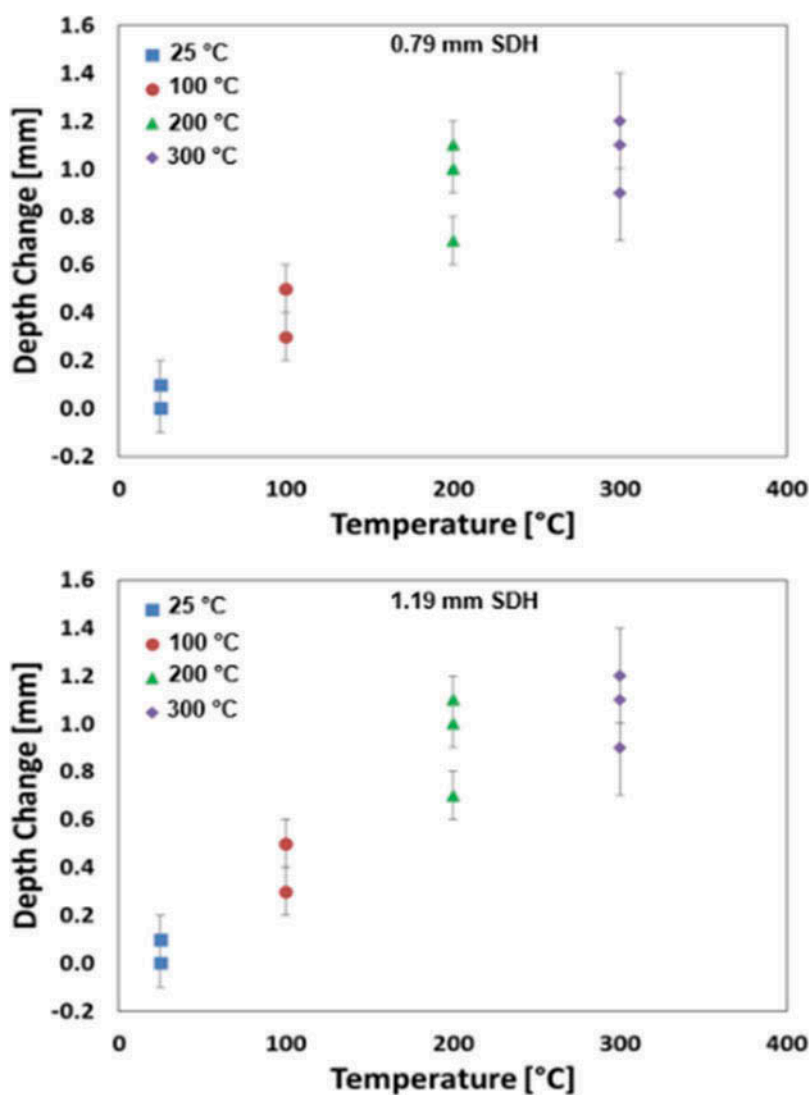
Figure 17. Effect of temperature on defect measurement for HT PAUT system for SDH of diameter 0.79 mm (top) and 1.19 mm (bottom).

compensate for these HTs with a change in material velocity. To improve this study, and to devise appropriate calibration procedures, further corrections must be determined experimentally for the material employed.

4.2. FSW fixture

A FSW fixture is a key factor in determining weld quality. The fixture rigidly holds the material to be welded in place and also acts as a heat sink. In order for the development of an online system, the HT wedge/transducer unit must fit between a bar which is used to clamp down the material (namely, chill bar)

and pin tool. An issue arises in many welding cases as the chill bar is typically placed very close to the weld seam which would not allow typical HT transducers found in the market available to be employed in this application (see Fig. 18 for a comparison of a typical industrial HT wedge, room temperature wedge, and newly developed HT wedge). This study is, to the author's knowledge, the first of its kind in that the HT/transducer unit was designed in consideration of the fixture geometries utilized in the aforementioned extensive AA-2219-T87 study (see Fig. 19). In later developments, depending on the geometry of the fixture and pin tool, the dimensions of the wedge/transducer setup can be adapted.

In order to utilize the current HT wedge/transducer setup, the chill bar on the AS was shifted from the nominal position of 1 inch from the weld seam to 3 inches to compensate for length of the HT wedge. This distance was considered safe to ensure that the wedge would not come into contact with
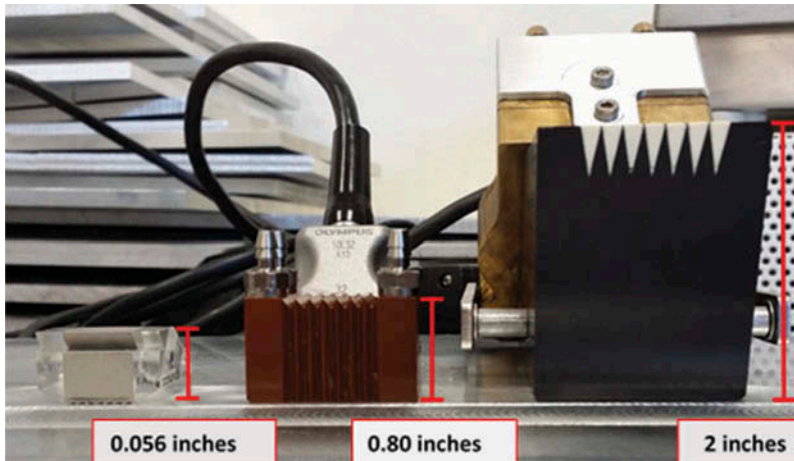
Figure 18. PAUT ambient temperature wedge (left), custom HT wedge, and commercial HT wedge.

Figure 19. Image of FSW fixture employed in this study.

the pin tool; however, moving the chill bar may result in a change in weld quality. The most obvious issue is that the workpiece will not be clamped as rigidly compared to the nominal position. Once the system is automated, the wedge/transducer unit will be closer to the weld seam allowing the chill bar to be placed closer. Further details of the effects of chill bar offset will follow in future studies.

4.3. Online PAUT during FSW

During welding experimentation, an I-Stir Process Development System (PDS) FS welder was employed to test the PAUT system. The experiment entailed placing the HT wedge/transducer unit roughly 25 mm away from the weld seam on the AS. This distance allowed enough clearance for the pin tool during welding, as can be seen in Fig. 20. The wedge/transducer unit was placed by hand to scan the workpiece before, during, and after the FSW fixed pin tool traversed the weld seam. A high-temperature couplant, called Pyrogel, which has an operating range of 315°C, was employed for HT tests. In a similar fashion, this method was conducted multiple times during each weld experiment. Four weld schedules were analyzed and can be observed in Table 4. The weld schedules chosen were conducted to obtain two nominal welds and two defect welds to observe the performance of the online PAUT system.

The above experiments confirmed that the PAUT HT wedge/transducer unit performed well. The wedge/transducer was able to assess the weld seam in the HT environment. At the start of the weld, the unwelded seam is clearly indicated in the S-scan image in Fig. 21(a). The high frequency waves reflecting off the wall have the appearance of a large defect. For the defect-

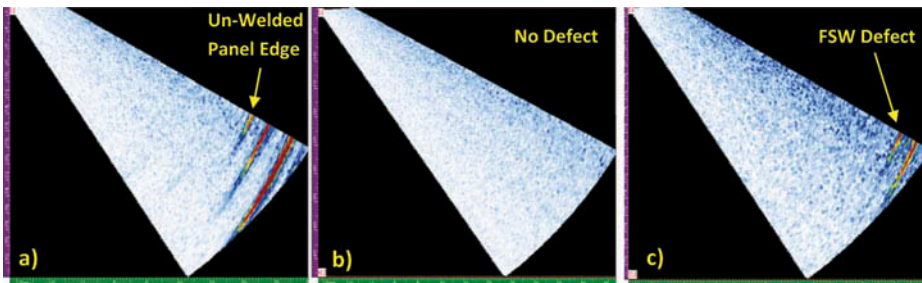**Figure 20.** Custom PAUT HT wedge/transducer unit scanning during FSW.

**Table 4.** FSW process parameters for online PAUT demos.

Weld Schedule	Rotational Speed [rpm]	Travel Speed [mm/min]	Plunge Force [kN]	UTS [MPa]	Quality
1	350	76.2	15.57	317.98	Nominal
2	300	152.4	26.69	324.83	Nominal
3	350	152.4	22.24	277.50	Defect
4	300	152.4	17.79	150.15	Defect

free experiments, once the pin tool traversed the weld seam, material was consolidated providing no defect signals. However, when defects are welded into the workpiece, the PAUT system is able to capture them. Figure 21 illustrates the S-scan images of the unwelded seam, nominal weld without defect, and weld with defect. As discussed previously, multiple legs are employed to scan the entire welded area. Consequently, care must be applied in interpreting the results as the distance for scanning in these experiments employed three legs, which can have adverse effects on correctly interpreting defect signals.

In image (c) of Fig. 21, only signals generated at large angles could determine the defect due to the distance the probe was placed from the weld seam, as indicated by Fig. 22. Here the first defect image was found by the second leg, and thereafter the second defect image was found by the third leg. The back-wall was not found in the image shown in Fig. 21 (b) due to the filter that was applied for scanning; moreover, as attenuation increased, the back-wall signal could not to be found. In Figs. 21(a) and (c), the back-wall is located at the same location of the defect, and hence it is hard to distinguish.

The above results indicate successful online NDE of FSW in real time. In this work, extensive calibration and testing was required to accurately utilize a custom wedge, HT scanning, and FSW fixture accommodation. In future work, progression to automate this system with an online scanning unit for real-time data acquisition will be conducted with further fine-tuning of

Figure 21. PAUT S-scan images of HT wedge/transducer unit signals: a) unwelded seam, b) nominal welded seam, and c) TR defect welded seam.
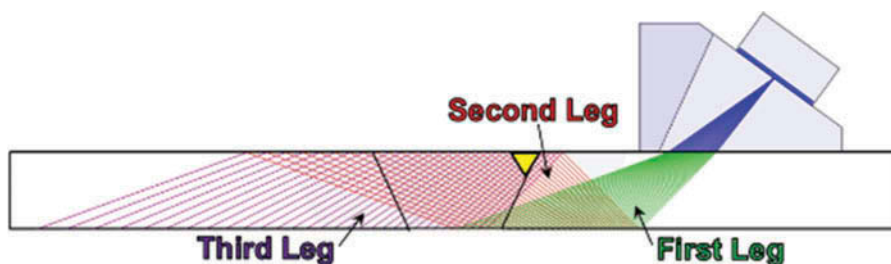
Figure 22. PAUT illustration of multiple legs scanning an FS welded with a TR defect on AS.

HTHT calibration techniques. Ultimately, the work provided in this study will cut down cost and delivery time for FSW manufacturing processes.

5. Conclusions

This article has presented a systematic study of PAUT for both post-weld and online inspection. Moreover, the capability of PAUT in detecting various forms of defective FS welds has been investigated and compared with X-ray radiography. One of the objectives of this study was to increase understanding of post-weld inspection with PAUT on FS-welded specimens. PAUT inspection is complex and requires significant time and understanding in order to be applied effectively. For these reasons, and due to a lack of literature of current PAUT methods on FS welds, a necessary study was conducted to illustrate the subtleties of PAUT operation with respect to the FSW technique. As the newly developed FSW process expands in industry, post-weld inspection will be heavily relied upon. It has been shown that the PAUT technique is an excellent choice for this undertaking and also more reliable than X-ray radiography. The importance of A-scan amplitude, index offset, TCG calibration, PAUT image analysis, and defect sizing were discussed. Furthermore, IP defects can be detrimental to aerospace industries as they are difficult to detect with PAUT and X-ray radiographic NDE techniques. IP defects can be discovered with increase in gain compared to the system calibrated for typical scanning procedures. Furthermore, successful implementation of a wedge/transducer unit for HTHT application has been shown. With an increase in temperature, PAUT software calibration is required to compensate for material property changes. For the first time, PAUT has been applied real time during FSW.

As the work progresses, an online scanning system will be developed and employed to automate NDE sensing of FSW which will greatly aid manufacturing processes. Another study will attempt to correlate welding schedules with defects for the purpose of predicting whether a defective weld will be produced for a certain welding setting and determining optimal friction stir welding conditions.

Acknowledgment

Funding

References

[1] A. Leonard and S. Lockyer. The 4th International Symposium on Friction Stir Welding. Park City, UT (2003).

[2] R. J. Ditchburn, S. K. Burke, and C. M. Scala. *NDT&E Int.* **29**:111–117 (1996).

[3] L. S. Rosado, T. G. Santos, M. Piedade, P. M. Ramos, and P. Vilaça. *Measurement* **43**:1021–1030 (2010).

[4] L. S. Rosado, F. A. Cardoso, S. Cardoso, P. M. Ramos, P. P. Freitas, and M. Piedade. *Sensor Actuat. A-Phys.* **212**:58–67 (2014).

[5] L. S. Rosado, T. G. Santos, P. M. Ramos, P. Vilaca, and M. Piedade. *NDT&E Int.* **51**:85–93 (2012).

[6] C. Mandache, D. Levesque, L. Dubourg, and P. Gougeon. *Sci. Technol. Weld. Join.* **17**:295–303 (2012).

[7] T. G. Santos, P. Vilaca, and R. M. Miranda. *J. Mater. Process. Manu.* **211**:174–180 (2011).

[8] T. G. Santos, P. Vilaca, J. dos Santos, and L. Quintino. *Weld. World* **53**:99–108 (2009).

[9] C. Mandache, L. Dubourg, A. Merati, and M. Jahazi. *Mater. Eval.* **66**:382–386 (2008).

[10] T. G. Santos, B. S. Silva, P. D. Vilaca, J. M. C. Sousa, and L. Quintino. *Soldagem Insp.* **12**:179–187 (2007).

[11] R. A. Smith. *Insight* **47**:133–143 (2005).

[12] G. Deuster. *Int. J. Pres. Ves. Pip.* **35**:173–188 (1988).

[13] D. Choqueuse and A. Lamarre. *Proceedings of the 8th International Offshore and Polar Engineering Conference.* ISOPE, Montreal, Canada (1998).

[14] P. Crowther. *Insight.* **46**:525–528 (2004).

[15] M. Moles, N. Dube, and F. Jacques. *Proceedings from Materials Solutions 2003 on Joining of Advanced and Specialty Materials.* ASM International, Pittsburgh, PA (2004).

[16] C. Schneider and C. Bird. The 4th European-American Workshop on Reliability of NDE. Berlin, Germany (2009).

[17] R. J. Ditchburn and M. E. Ibrahim. *Ultrasonic Phased Arrays for the Inspection of Thick-Section Welds.* Australian Department of Defense Science and Technology Organization, Victoria, Australia (2009).

[18] Olympus Corporation. *Introduction to Phased Array Ultrasonic Technology Applications: R/D Tech Guideline.* 1st ed. Olympus NDT, Waltham, MA (2004).

[19] Olympus Corporation. *Advances in Phased Array Ultrasonic Technology Applications,* Olympus NDT, Waltham, MA (2007).

[20] W. Shi-Chang and S. Yijun. *Wave Motion* **29**:245–265 (1999).

[21] W. D. Bruce and D. W. Paul. *NDT&E Int.* **39**:525–541 (2006).

[22] L. R. Joseph. *J. Press. Vess. T. ASME* **124**:273–282 (2002).

[23] J. L. Rose. *IEEE Trans. Ultrason. Ferr.* **47**:575–583 (2000).

[24] J. L. Rose. *Ultrasonic Waves in Solid Media*. Cambridge University Press, Cambridge, UK (1999).

[25] L. Azar, Y. Shi, and S. C. Wooh. *NDT&E Int.* **33**:189–198 (2000).

[26] D. Achenbach. *Wave Propagation in Elastic Solids*. North-Holland Publishing Co., New York, NY (1984).

[27] B. A. Auld. *Acoustic Fields and Waves in Solids*. 2nd ed. Vol. 2. Krieger Publishing Co., Malabar, FL (1990).

[28] L. W. Schmmer. *Mod. Phys., Lett. B.* **22**:917–921 (2008).

[29] A. S. Birks, R. E. J. Green, and P. McIntire. *Nondestructive Testing Handbook*. 2nd ed. Ultrasonic Testing. Vol. 7. American Society for Nondestructive Testing, Columbus, OH (1991).

[30] B. Li, Y. Shen, and W. Hu. *Material Design* **32**:2073–2084 (2011).

[31] C. Carpentier and J. Rudlin. The 11th European Conference on Non-Destructive Testing. Prague, Czech Republic (2014).

[32] M. W. Dewan, D. J. Huggett, T. W. Liao, M. A. Wahab, and A. M. Okeil. *Material Design* **92**:288–299 (2015).

[33] Olympus Corporation. *Flaw Detectors OmniScan MX2*. Available at http://www.olympus-ims.com/en/omniscan-mx2/ (accessed 11 December, 2015).

[34] A. Lamarre, O. Dupuis, and M. Moles. *Proceedings of the 7th International Conference on Trends in Welding Research*. Callaway Gardens Resort, Pine Mountain, GA (2005).

[35] C. R. Bird. *Insight* **46**:31–36 (2004).

[36] D. Kleiner and C. R. Bird. *Insight* **46**:85–87 (2004).

[37] D. Levesque, L. Dubourg, and A. Blouin. *Nondestructive Test Eval.* **26**:319–333 (2011).

[38] K. J. Kirk, A. McNab, A. Cochran, I. Hall, and G. Hayward. *IEEE Trans. Ultrason. Ferr.* **46**:311–319 (1999).

[39] R. Subbaratnam, S. T. Abraham, M. Menaka, B. Venkatraman, and B. Raj. *Mater. Eval.* **66**:332–337 (2008).

[40] W. Johnson, F. Mauer, D. Pitchure, S. J. Norton, Y. Grinberg, and F. Bendec. *J. Mater. Res.* **8**:1558–1566 (1993).

[41] J. L. Shih, K. T. Wu, C. K. Jen, C. H. Chiu, J. C. Tzeng, and J. W. Liaw. *Sensors* **13**:975–983 (2013).

[42] F. Tariq, N. Naz, R. Baloch, and Faisal. *J. Nondestruct. Eval.* **31**:17–33 (2012).

[43] E. Oberg, F. Jones, H. Horton, and H. Ryffel. *Temper Designations for Aluminum Alloys in Machinery's Handbook*. 29th ed. Industrial Press, New York, NY (2012).

[44] ASME, Article 23 Ultrasonic Standards, in SE-797. *The Standard Practice for Measuring Thickness by Manual Ultrasonic Pulse-Echo Contact Method*. (1998).